

# Facile fabrication of heterostructure with p-BiOCl nanoflakes and n-ZnO thin film for UV photodetectors

Longxing Su<sup>1,2</sup>, Weixin Ouyang<sup>1</sup>, and Xiaosheng Fang<sup>1,†</sup>

<sup>1</sup>Department of Materials Science, Fudan University, Shanghai 200433, China

<sup>2</sup>Department of Physical Science and Technology, ShanghaiTech University, Shanghai 200433, China

**Abstract:** Herein, high-quality n-ZnO film layer on *c*-sapphire and well-crystallized tetragonal p-BiOCl nanoflakes on Cu foil are prepared, respectively. According to the absorption spectra, the bandgaps of n-ZnO and p-BiOCl are confirmed as ~3.3 and ~3.5 eV, respectively. Subsequently, a p-BiOCl/n-ZnO heterostructural photodetector is constructed after a facile mechanical bonding and post annealing process. At -5 V bias, the photocurrent of the device under 350 nm irradiation is ~800 times higher than that in dark, which indicates its strong UV light response characteristic. However, the on/off ratio of In-ZnO-In photodetector is ~20 and the Cu-BiOCl-Cu photodetector depicts very weak UV light response. The heterostructure device also shows a short decay time of 0.95 s, which is much shorter than those of the devices fabricated from pure ZnO thin film and BiOCl nanoflakes. The p-BiOCl/n-ZnO heterojunction photodetector provides a promising pathway to multifunctional UV photodetectors with fast response, high signal-to-noise ratio, and high selectivity.

**Key words:** ZnO thin film; BiOCl nanoflakes; heterostructure; UV photodetector

**Citation:** L X Su, W X Ouyang, and X S Fang, Facile fabrication of heterostructure with p-BiOCl nanoflakes and n-ZnO thin film for UV photodetectors[J]. *J. Semicond.*, 2021, 42(5), 052301. <http://doi.org/10.1088/1674-4926/42/5/052301>

## 1. Introduction

UV photodetectors have received considerable attention in recent years thanks to their broad range of applications, including environmental monitoring, space communication, biological sensing and missile plume sensing<sup>[1–6]</sup>. UV photodetectors are classified as three types: photoconductive type photodetectors, Schottky type photodetectors, and p–n junction type photodetectors<sup>[3]</sup>. Generally, photoconductive-type photodetectors show high responsivity because of the internal gains. However, the dark current of this type of device is very high and the response time of the photodetector is quite slow because of the surface defect states<sup>[7, 8]</sup>. Schottky type photodetectors with Schottky contact electrodes usually present a rapid response. However, the depletion layer depth in Schottky junction is very shallow and the Schottky barrier height is influenced by the surface states. Hence, precise control of the interface between contacted electrode and semiconductor is required. P–n junction type photodetectors with both rapid response speed and superior responsivity have great potential for use in commercial applications. However, the device assembly processes (e.g., photolithography, etching, and metal evaporation) are complicated and expensive. Thus, a low-cost facile fabrication method is highly desirable to realize scalable and high-performance p–n junction UV photodetectors.

UV photodetectors fabricated with wide bandgap materials have been widely investigated and reported, such as Ga<sub>2</sub>O<sub>3</sub><sup>[9–12]</sup>, GaN<sup>[13–15]</sup>, TiO<sub>2</sub><sup>[16, 17]</sup>, NiO<sup>[18, 19]</sup>, CuZnS<sup>[20, 21]</sup>, ZnO<sup>[22–26]</sup> and so on. In particular, attentions has been given

to develop ZnO-based UV photodetectors due to their superior properties such as low preparation cost, wide direct bandgap, biocompatibility, and strong radiation hardness<sup>[27, 28]</sup>. To date, UV photodetectors prepared with ZnO thin films, nanoparticles and nanowires have been intensively reported. However, because of the abundant surface defects in the material, the response speeds of these photodetectors are extremely slow (typically at a scale of tens of seconds or even several minutes). Therefore, constructing a suitable p–n junction to separate the photogenerated electron–hole pairs may be an appropriate choice to improve the key performance parameter. Because p-ZnO is rather difficult to be prepared, ZnO-based p–n homojunction photodetectors are rarely reported<sup>[29, 30]</sup>. Moreover, the stability of the as-prepared p-ZnO material is still out of reach and it may lead to the failure of the device. Therefore, most attempts are focused on ZnO-based heterostructure photodetectors. Hu *et al.* prepared a p-Se/n-ZnO hybrid UV photodetector and greatly reduced the response time to microseconds<sup>[31]</sup>. The response time is much faster than that of pure ZnO photodetectors, which is mainly ascribed to the built-in electric field in p-Se/n-ZnO heterojunction. A p-type conducting polymer (polyaniline, PANI) was utilized as the hole transport layer to fabricate an organic/inorganic heterostructure deep-UV photodetector<sup>[32]</sup>. The device's response time is reported to be less than 0.3 s. Therefore, seeking an appropriate p-type material to hybrid with n-ZnO is an urgent and valid way to improve the response time of the device.

Bismuth oxyhalides are ternary alloy semiconductors with a chemical expression of [Bi<sub>2</sub>O<sub>m</sub>X<sub>n</sub>], where X = I, Cl, or Br<sup>[33]</sup>. They have been widely reported as catalysts, cosmetics, ferroelectric materials and photoelectrochemical materials because of their superior catalytic and optoelectronic characteristics<sup>[34–39]</sup>. In particular, they have specific layered crystal

Correspondence to: X S Fang, [xshfang@fudan.edu.cn](mailto:xshfang@fudan.edu.cn)

Received 21 SEPTEMBER 2020; Revised 19 OCTOBER 2020.

©2021 Chinese Institute of Electronics

structures, which the positive slabs are composed by  $[\text{Bi}_2\text{O}_2]^{2+}$ , while the negative slabs along  $c$ -axis are composed by halide atoms<sup>[40]</sup>. Thus, the self-induced built-in electric field generates and then contributes to the efficient collection of photogenerated carriers<sup>[41]</sup>. Typically, the bandgap of bismuth oxychloride (BiOCl) changes from 3.0 to 3.8 eV, which leads to its great potential in UV photodetectors<sup>[42]</sup>. In addition, the as-prepared BiOCl nanostructure naturally exhibits  $p$ -type characteristic. Therefore, constructing a  $p$ - $n$  heterojunction that is composed of  $p$ -BiOCl nanoflakes and  $n$ -ZnO thin film can help to improve the performance of ZnO-based photodetectors.

Herein, we report a photodetector by constructing a heterojunction with high-quality  $n$ -type ZnO thin film and  $p$ -type BiOCl nanoflakes. A noticeable rectification characteristic is observed through the  $I$ - $V$  curves in dark, indicating the successful formation of a heterojunction. The photodetector demonstrates excellent UV light selectivity and its on/off ratio ( $I_{350\text{ nm}}/I_{\text{dark}}$ ) reaches as high as 800. However, the on/off ratio of  $\text{In-ZnO-In}$  photodetector and  $\text{Cu-BiOCl-Cu}$  photodetector are  $\sim 20$  and less than 2, respectively. The improvement is ascribed to the more efficient separation of photo-excited carriers forced by the built-in electric field. The device also demonstrates shorter response time (rise time of 12.6 s, decay time of 0.95 s) than those devices fabricated on pure  $n$ -ZnO and  $p$ -BiOCl. This low-cost fabrication strategy of constructing ZnO-film-based  $p$ - $n$  heterostructure envisages a profound impact on the next generation ZnO-based photodetectors.

## 2. Experimental

### 2.1. Preparation of ZnO thin film on sapphire substrate

We utilized the RF (radio frequency) plasma assisted molecular beam epitaxy (MBE) technique to synthesize the ZnO film layer. Prior to the growth of ZnO, the substrate and Zn source were preheated to 650 and 340 °C, respectively. In the growth process, the flux rate of oxygen was steadied at 120 sccm, the RF power was kept at 400 W.

### 2.2. Preparation of BiOCl nanoflakes on Cu foil

0.1577 g of  $\text{BiCl}_3$  and 3.3 mL of concentrated HCl were added into 95 mL mixture solvent of ethylene glycol and  $\text{H}_2\text{O}$  (volume ratio: 10 : 85). After the mixed solution was stirred and heated to 70 °C, 1 mL of 30%  $\text{H}_2\text{O}_2$  solution was added into this solution. Then, a piece of clean copper foil was immersed into this solution for 1 h. After being washed by absolute alcohol three times, and then dried at 60 °C for 1 h, the obtained sample was kept in a storage for further use. We bought all these chemical reagents from the Sinopharm Company and they were used as received.

### 2.3. Characterization

To investigate their crystal structures and quality, we acquired the X-ray diffraction (XRD) patterns of the samples by a Bruker D8-A25 diffractometer using  $\text{Cu K}\alpha$  radiation ( $\lambda = 1.5405 \text{ \AA}$ ). The absorption spectra were recorded on a Hitachi U3900H UV-Vis-NIR scanning spectrophotometer. The morphologies and microstructures of the samples were examined by a field-emission scanning electron microscopy (FESEM) from Zeiss Sigma company and a high-resolution transmission electron microscopy (HRTEM) from TECNAI company, respectively. We employed an atomic force microscope from Bruker company to characterize the surface properties of ZnO

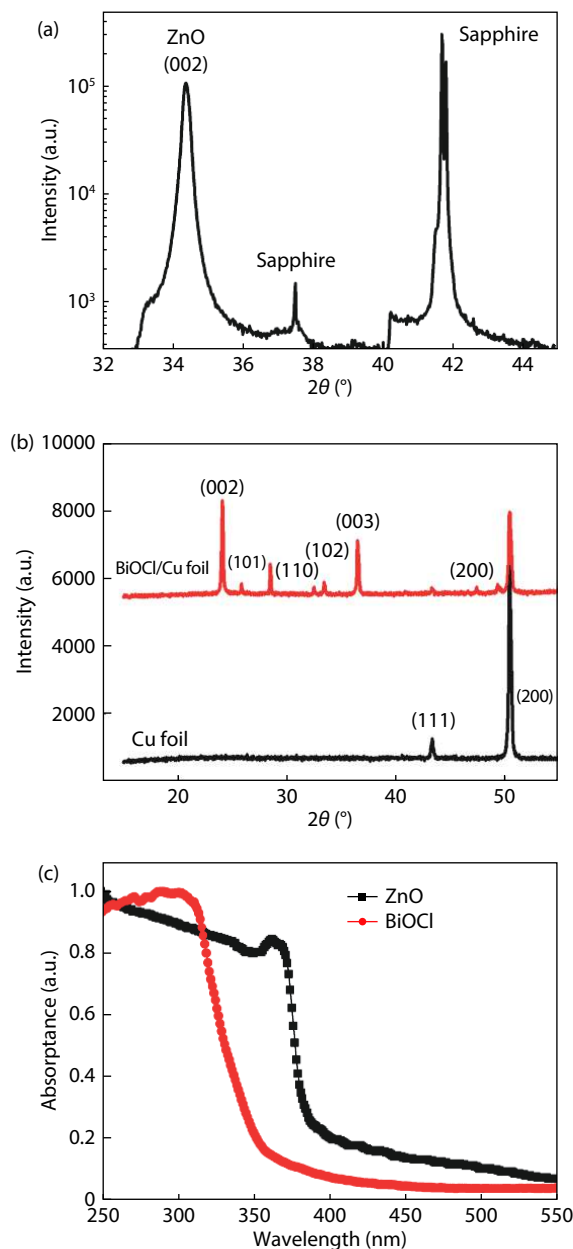


Fig. 1. (Color online) (a) XRD pattern of ZnO thin film. (b) XRD patterns of BiOCl on Cu foil substrate and Cu foil. (c) Optical absorption spectra of BiOCl nanoflakes and ZnO thin film.

film layer.

### 2.4. Device fabrication and photoelectric measurement

The  $p$ -BiOCl/ $n$ -ZnO heterostructured photodetector was prepared by mechanical bonding of two different materials and then annealed at 100 °C for 0.5 h. Cu foil and metal Indium pad were used as the electrodes to contact with the  $p$ -BiOCl and  $n$ -ZnO, respectively. The photoelectric performance of the as-constructed device was studied through a Xe lamp equipped with monochromator as the light source, and a Keithley 4200 semiconductor characterization system as the analyzer. A NOVA II power meter from OPHIR photonics was utilized to measure the optical power density-wavelength curve of the light source. We conducted all of the measurements in air ambient.

## 3. Results and discussion

Fig. 1(a) illustrates the XRD results of ZnO film layer on sap-

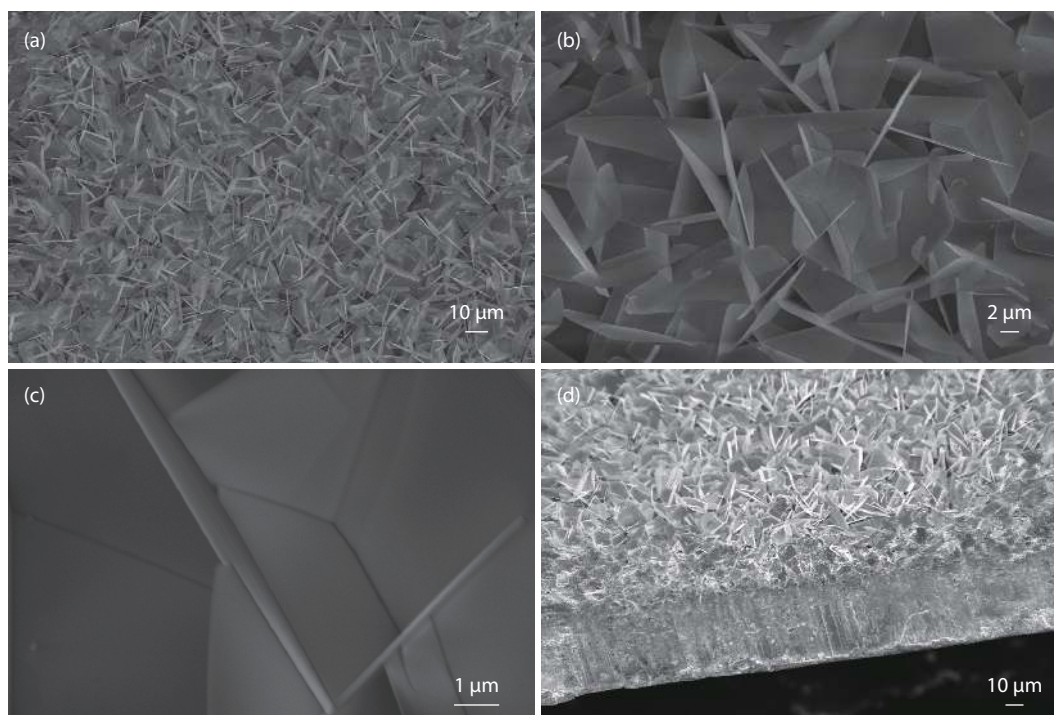


Fig. 2. SEM images of BiOCl on Cu foil at different levels of magnification.

phire substrate. Apart from the characteristic diffraction peaks from the sapphire substrate, only one diffraction peak centered at around  $34.4^\circ$  is found. This peak originates from the (002) diffraction signal of wurtzite ZnO and reveals its  $c$  direction growth preference. The full width at half maximum (FWHM) of this peak is only  $0.22^\circ$ . Fig. 1(b) displays the XRD results of the BiOCl nanoflakes on Cu foil and Cu foil, it is seen that all the main diffraction peaks from the obtained BiOCl sample on Cu foil are indexed to the (002, 110, 102, 003, and 200) facets of tetragonal BiOCl (JCPDS No. 6-249). Two weak diffraction peaks that resulted from the byproducts and residual of reactants are also detected. The sharp and intense diffraction peaks suggest that the as-synthesized BiOCl sample is well-crystallized. In addition, the intensity of the diffraction peaks from (002) and (003) facets are stronger than the peak intensities of the other facets, which may indicate the favored growth orientations of the BiOCl. To estimate the bandgaps of these materials, optical absorption spectra of BiOCl sample and ZnO thin film are tested. Fig. 1(c) presents the normalized absorption spectra of BiOCl and ZnO, the absorption edges of both materials are located at the UVA range. The cut-off absorption edge located at  $\sim 375$  nm can be ascribed to the ZnO film layer and the cut-off absorption edge at  $\sim 345$  nm is ascribed to the BiOCl nanoflakes. Therefore, the bandgaps of the as prepared ZnO and BiOCl materials are confirmed as  $\sim 3.3$  and  $\sim 3.5$  eV.

Fig. 2 reveals the morphology and crystal structures of BiOCl nanoflakes. From the top view scanning electron microscopy (SEM) images in Figs. 2(a) and 2(b), it can be seen that the BiOCl nanoflakes are homogeneously and densely grown on the entire surface of Cu foil, neighboring nanoflakes are connected with each other to form arrays. From the magnified SEM image in Fig. 2(c), the individual nanoflakes present even and smooth dominant surfaces and their thicknesses are estimated to be several tens of nanometers.

The side view SEM pattern of BiOCl nanoflakes on Cu foil is illustrated in Fig. 2(d), and a distinct and coarse boundary between the BiOCl nanoflakes and the Cu foil is presented. The average height of the BiOCl nanoflake arrays is estimated to be  $\sim 20$   $\mu\text{m}$ . Fig. 3 presents the surface fluctuation of the ZnO film layer. The root-mean-square roughness over  $5 \times 5$   $\mu\text{m}^2$  area is only  $\sim 0.85$  nm and the section profile (white line in Fig. 3(a)) shown in Fig. 3(b) indicates that the maximum surface fluctuation is  $< 1.2$  nm. 3D atomic force microscopy (AFM) image of the ZnO film layer (Fig. 3(c)) presents the homogenous distribution of hexagonal pyramids. The AFM measurement indicates a smooth surface morphology of the ZnO film layer prepared by MBE. The dense distribution and conformal coverage of the BiOCl nanoflake arrays on the Cu foil and the smooth surface of ZnO thin film can ensure their intimate contact after the post annealing process, which is beneficial for the carrier transport in the heterostructure photodetector.

Fig. 4(a) shows a transmission electron microscopy (TEM) image of the BiOCl nanoflakes on Cu foil substrate. Here, the BiOCl nanoflakes sample was scraped down and then transferred to the Cu mesh for the TEM measurement. The nanoflake's surface presents flat and uniform properties. The clear lattice fringes in high-resolution TEM (HRTEM) image (Fig. 4(b)) illustrates the high crystal quality of the nanoflake prepared by this chemical bath method. The interplanar lattice spacing is 0.275 nm, corresponding to the (110) planes of tetragonal BiOCl. In addition, the selected-area electron diffraction (SAED) measurement (Fig. 4(c)) indicates the single-crystalline property of the BiOCl nanoflakes. A  $45^\circ$  angle is labeled between two sets of SAED spots, which perfectly agrees well with the angle between (200) and (110) planes. These diffraction spots can be confirmed as the [001] zone axis of tetragonal BiOCl. In addition, considering the crystal symmetries of BiOCl and the previous results, the dominant sur-

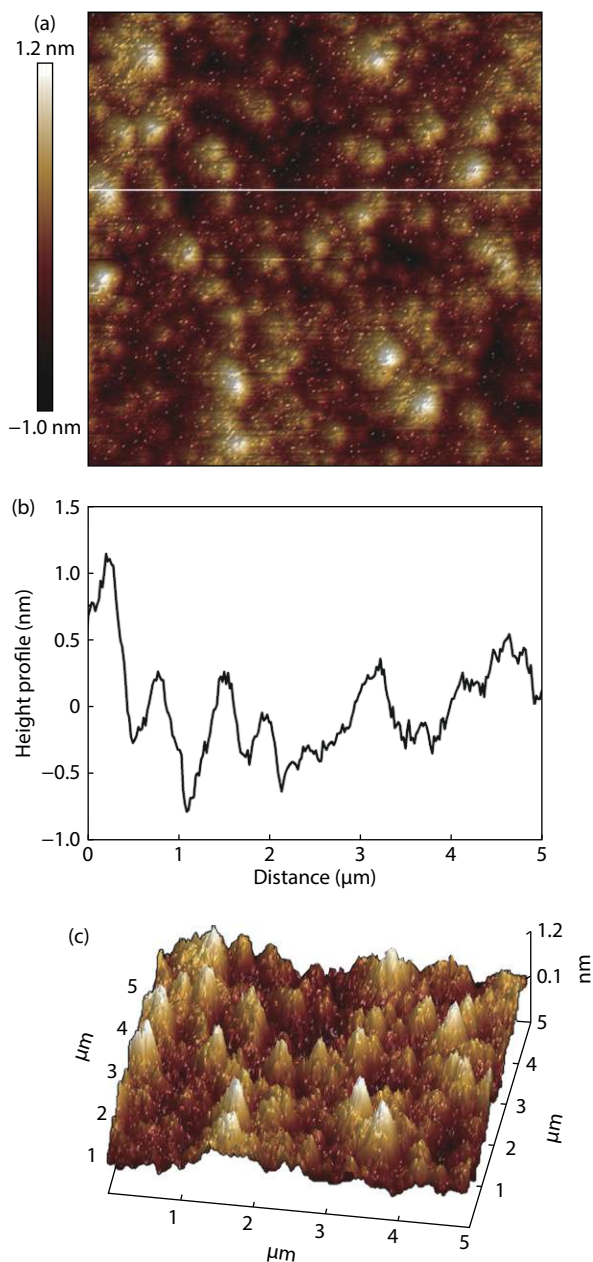


Fig. 3. (Color online) (a) Top view AFM image of ZnO thin film at a scale of  $5 \times 5 \mu\text{m}^2$ . (b) Section profile of ZnO thin film. (c) 3D AFM image of ZnO thin film.

face of the BiOCl nanoflakes is identified as (001) facet.

The photoelectric characteristics were systematically studied by employing a two-probe technique in ambient. The device configuration is shown in Fig. 5(a). Metal indium pad is utilized to prepare an Ohmic contact with ZnO, the Cu foil naturally achieves an Ohmic contact with the BiOCl nanoflakes. Both metal indium pad and Cu foil are bonded with Cu wires and then connected with two probes. In this configuration, the incident light is irradiated from the back side where the sapphire ( $E_g \sim 7.6$  eV) substrate can act as a transparent window to the incident light. As revealed in Fig. 5(c), the  $I$ - $V$  curve recorded in the dark illustrates that this as-fabricated photodetector features a rectifying characteristic. The turn-on voltage is  $\sim 3.2$  V and the ratio is  $\sim 66$  at  $\pm 4$  V biases. For comparison, an In-ZnO-In device consisting of ZnO film and two pieces of indium pads as electrodes, and a Cu-BiOCl-Cu device consisting of BiOCl nanoflakes and two

pieces of Cu foils as electrodes were fabricated. Figs. 5(b) and 5(d) present the  $I$ - $V$  results of In-ZnO-In device and Cu-BiOCl-Cu device in dark, respectively. It is clearly shown that both currents have a linear correlation with the voltages. Hence, the contacts between indium pads and ZnO film, as well as the contacts between BiOCl nanoflakes and Cu foil are Ohmic contacts. Therefore, the rectifying characteristic of the photodetector originates from the p-BiOCl/n-ZnO heterojunction. The effects of Schottky junction between semiconductors and metal electrodes on the rectifying characteristic can thus be excluded. The inset of Fig. 5(c) presents the  $I$ - $V$  curves under dark and UV light irradiation (350 nm). Under  $-5$  V bias, the photocurrent value under 350 nm light irradiation is  $\sim 800$  times of that in dark, which indicates that the p-BiOCl/n-ZnO device shows a strong response to UV light. However, for In-ZnO-In photoconductive device, the on/off ratio at 350 nm is only  $\sim 20$ . In addition, the Cu-BiOCl-Cu photoconductive device has a very weak response to UV light. Therefore, it is concluded that the strong response of p-BiOCl/n-ZnO photoconductor to UV light is due to the characteristics of the heterostructure.

Responsivity ( $R_\lambda$ ) is a key parameter to estimate the sensitivity of the photodetector. It can be calculated by the equation of  $R_\lambda = (I_\lambda - I_d)/P_\lambda S$ , where  $I_\lambda$ ,  $I_d$  and  $S$  are the photocurrent and dark current of the device's effective area under irradiation, respectively. Fig. 6 presents the spectral responsivities of p-BiOCl/n-ZnO heterostructure photodetector under different biases. A clear cut-off wavelength at around 380 nm is found, which corresponds well with the absorption edge of ZnO. In addition, the responsivity increases as the external bias increases and the maximum responsivity under  $-5$  V is  $\sim 0.15$  A/W. This indicates that the active layer of the device under negative biases is mainly located on the ZnO side. It is worth noting that the spectral response curves (Fig. 6(b)) at positive biases are different from those under negative biases (Fig. 6(a)). Additional weak response signals found at around 320 nm are ascribed to the intrinsic photoresponse of BiOCl nanoflakes. The different responsivities under negative and positive biases can be ascribed to the variation of the depletion layer depth. As the positive bias increases, the depletion layer depth decrease because of the inner potential offset. Therefore, the equivalent circuit of p-BiOCl/n-ZnO photodetector can be regarded as a series of BiOCl photosensitive resistors, p-n junctions, and ZnO photosensitive resistors. Because the BiOCl nanoflakes are well-aligned on the surface of the Cu foil, the photogenerated carriers in BiOCl photosensitive layer can be easily collected and effectively contributed to the photocurrent. Thus, intrinsic response of BiOCl nanoflakes is shown under positive biases. Typically, the detectivity  $D^*$  demonstrates the noise equivalent power (NEP) in a device and can be defined as:  $D^* = R_\lambda(2eI_d/S)^{-1/2}$ , where  $e$  is the elementary charge constant. Fig. S1 depicts the wavelength dependent detectivity of p-BiOCl/n-ZnO UV photodetector at different bias voltages. Obviously, the device shows high detectivity of  $> 10^{11}$  Jones at different bias voltages, which demonstrates the device's excellent capability to detect signals from noise environment. Fig. 6(c) presents the energy band diagram of the p-BiOCl/n-ZnO heterostructure, where a type-II band structure is formed. Thus, the as-generated built-in electric field can effectively separate the photo-induced electron-hole pairs, contributing to the superior per-

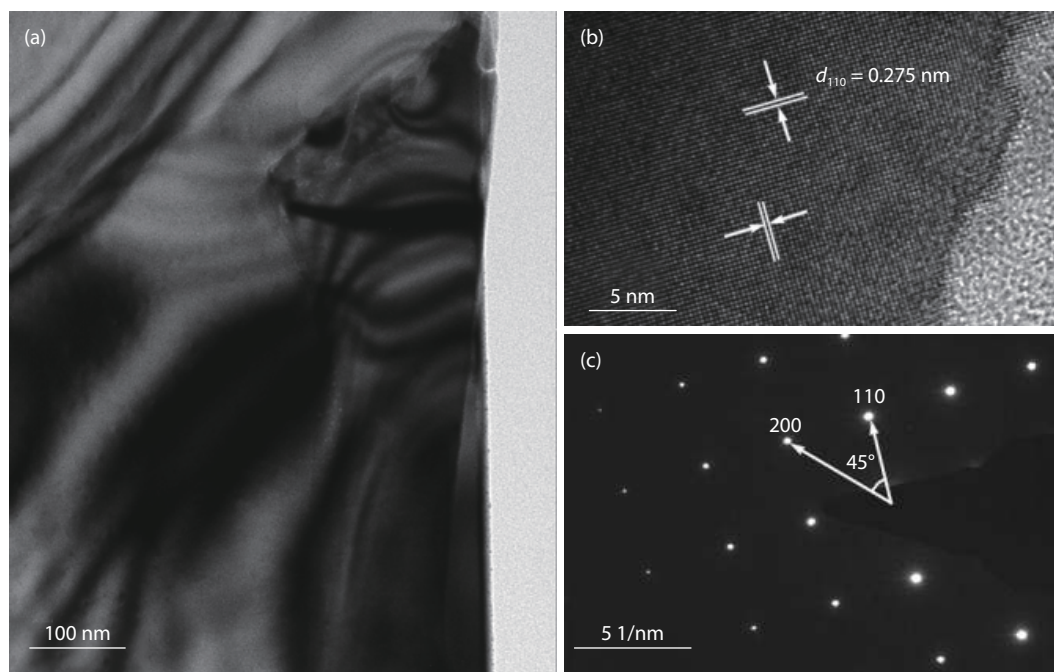


Fig. 4. (a) TEM image, (b) HRTEM image, and (c) SAED pattern of the BiOCl nanoflakes samples.

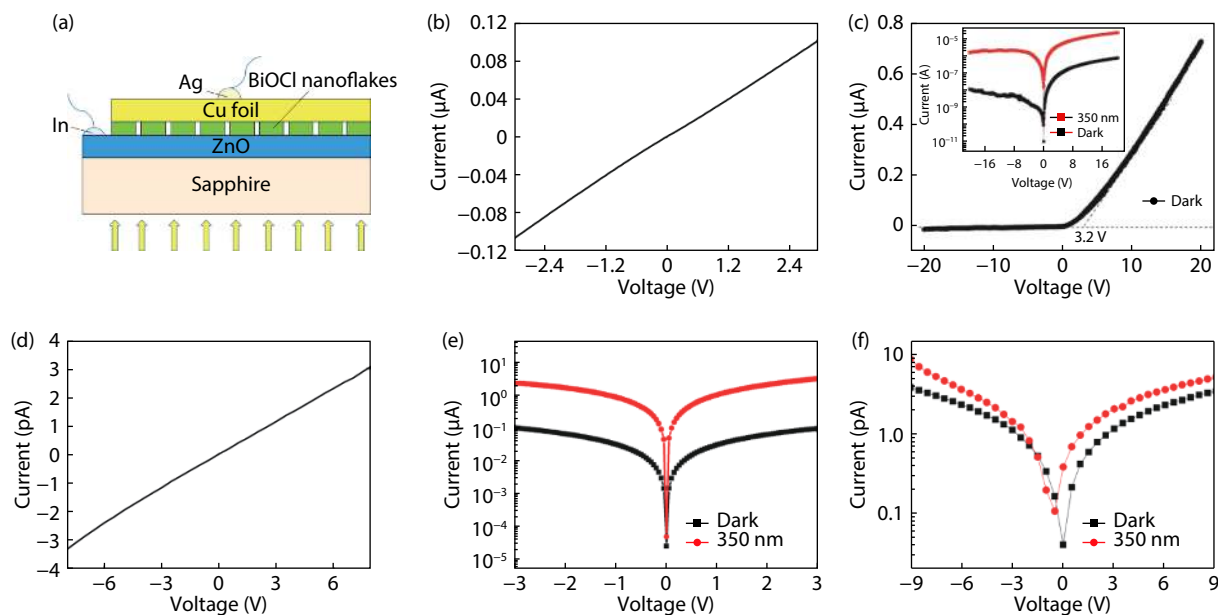


Fig. 5. (Color online) (a) Schematic diagram of the p-BiOCl/n-ZnO photodetector with back-side light irradiation. (b)  $I$ - $V$  curve of In-ZnO-In device in dark. (c)  $I$ - $V$  curve of p-BiOCl/n-ZnO photodetector in dark, inset is the  $I$ - $V$  curves of the device in dark and under 350 nm light illumination at logarithmic scale. (d)  $I$ - $V$  curve of Cu-BiOCl-Cu device in dark. (e) Logarithmic scale  $I$ - $V$  curves of In-ZnO-In device in dark and under 350 nm light illumination. (f) Logarithmic scale  $I$ - $V$  curves of Cu-BiOCl-Cu device in dark and under 350 nm light illumination.

formance of the photodetector, and even making the photodetector operate under 0 V bias. Figs. S2 and S3 present the photoresponse of this heterostructure device under 0 V bias, from which the photodetector is deemed as a self-powered device. However, the photodetector shows relatively poor performance without external bias voltage, mainly because of the mechanical contacted interface between p-BiOCl and n-ZnO. Further strategies such as directly grown p-BiOCl nanoflakes on n-ZnO film layer can be considered to improve the hetero-interface, and thus the photodetector can work as a high performance photovoltaic type device.

Fig. 7(a) displays the on/off switching current states of p-

BiOCl/n-ZnO photodetector under 350 nm ( $0.304 \text{ mW/cm}^2$ ), 400 nm ( $0.386 \text{ mW/cm}^2$ ), and 450 nm ( $0.426 \text{ mW/cm}^2$ ) light illuminations at  $-3 \text{ V}$ , respectively. Although the optical power density increases, the photocurrent decreases as the irradiation wavelength increases. The dark current nearly coincides with the photocurrent under 450 nm light illumination, indicating the excellent UV light selectivity of this device. According to the  $I$ - $T$  curve shown in Fig. 7(b), the rise time (from 10% to 90% of the maximum current) and decay time (from 90% to 10% of the maximum current) are calculated as 12.6 and 0.95 s, respectively. Typically, owing to the surface states caused by the defects like oxygen vacancies, ZnO

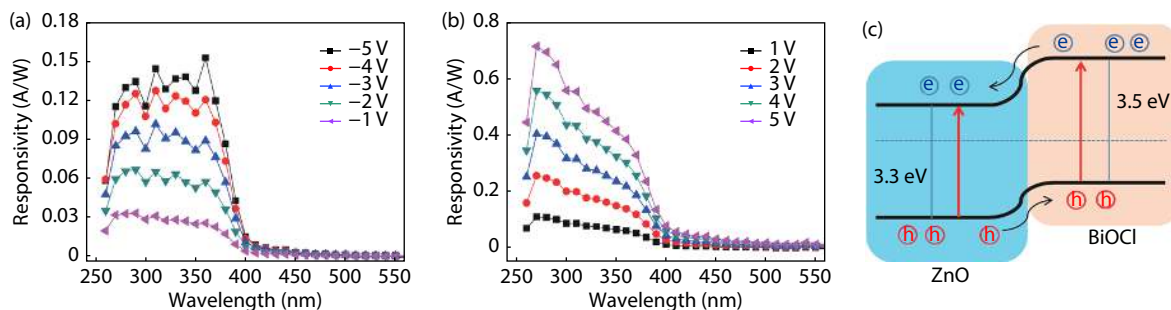


Fig. 6. (Color online) The photoresponse spectra of the p-BiOCl/n-ZnO photodetector at different (a) negative biases and (b) positive biases. (c) Schematic energy band diagram of the device.

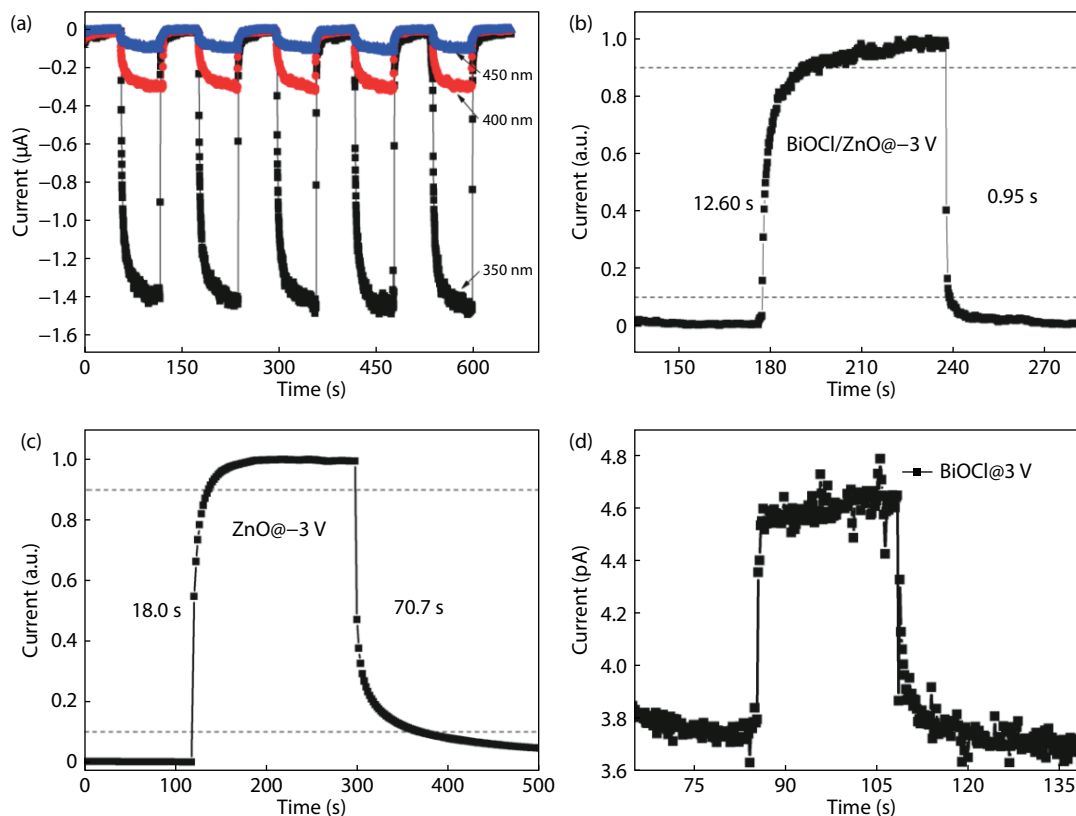


Fig. 7. (Color online) (a) Time response (“on” and “off” states) characteristic of the p-BiOCl/n-ZnO photodetector under 350 nm ( $0.304 \text{ mW/cm}^2$ ), 400 nm ( $0.386 \text{ mW/cm}^2$ ), and 450 nm ( $0.426 \text{ mW/cm}^2$ ) light illumination at  $-3 \text{ V}$ . (b) Normalized time response of the p-BiOCl/n-ZnO photodetector under 350 nm ( $0.304 \text{ mW/cm}^2$ ) illumination at  $-3 \text{ V}$ . (c) Single period time response of the In-ZnO-In photodetector under 350 nm ( $0.304 \text{ mW/cm}^2$ ) illumination at  $-3 \text{ V}$ . (d) Single period time response of the Cu-BiOCl-Cu photodetector under 350 nm ( $0.304 \text{ mW/cm}^2$ ) illumination at  $3 \text{ V}$ .

based photoconductive-type photodetector exhibits extremely slow response time (typically several minutes). As presented in Fig. 7(c), the response time of the In-ZnO-In photoconductive device are calculated to be 18 s (rise time) and 70.7 s (decay time). Thus, the decay speed of the p-BiOCl/n-ZnO photodetector is almost 74 times faster than that of the In-ZnO-In photoconductive device. Here, the tiny improvement of rise time results from the relatively incomplete mechanical contact between p-BiOCl and n-ZnO. Due to a low on/off ratio of 1.15 (Fig. 7(d)), the response time of Cu-BiOCl-Cu photoconductive device could not be calculated. In general, the response speed is significantly improved through the formation of a p-BiOCl/n-ZnO heterojunction.

#### 4. Conclusion

In conclusion, a novel UV photodetector constructed with the n-type ZnO thin film and p-type BiOCl nanoflakes is successfully realized through a facile fabrication process. The wurtzite n-ZnO thin film with preferred *c*-axis growth direction and low concentration of defects is prepared by MBE on a *c*-sapphire substrate, while the p-BiOCl nanoflakes are grown on a Cu foil by a simple chemical bath technique. Subsequently, this heterostructure photodetector is assembled through mechanical bonding and post-annealing of two materials. The p-BiOCl/n-ZnO device exhibits a high UV-visible rejection ratio of  $10^2$  and a faster response time than those of pure ZnO and BiOCl based photodetectors. In addition, the on/off ratio of the photodetector achieves as large as 800 un-

der  $-5$  V, which is also much higher than those of pure ZnO and BiOCl based photodetectors. This work provides an effective and facile way for preparing high performance heterostructure photodetectors, suggesting its potential applications in future optoelectronic devices.

## Acknowledgements

Dr. Longxing Su and Dr. Weixin Ouyang contributed equally to this work. The authors would like to thank Dr. Xiaojie Xu and Miss Yihan Chen for their kind help.

This work is supported by the National Natural Science Foundation of China (Grant No. 61705043, 51872050 and 11811530065), the National Key Research and Development Program of China (Grant No. 2017YFA0204600), the Natural Science Foundation of Jiangsu Province (No. BK20160568); National Postdoctoral Science Foundation of China (Grant No. 2017M611411, 2018M640338, 2018T110344 and 2019T120299) and the Ministry of Education Joint Fund for Equipment Pre-Research (6141A02033241).

## Appendix A. Supplementary materials

Supplementary materials to this article can be found online at <https://doi.org/1674-4926/42/5/052301>.

## References

- Chen H Y, Liu K W, Hu L F, et al. New concept ultraviolet photodetectors. *Mater Today*, 2015, 18(9), 493
- Lou Z, Yang X L, Chen H R, et al. Flexible ultraviolet photodetectors based on ZnO-SnO<sub>2</sub> heterojunction nanowire arrays. *J Semicond*, 2018, 39(2), 024002
- Su L X, Yang W, Cai J, et al. Self-powered ultraviolet photodetectors driven by built-in electric field. *Small*, 2017, 13(45), 1701687
- Xu X J, Chen J X, Cai S, et al. A real-time wearable UV-radiation monitor based on a high-performance p-CuZnS/n-TiO<sub>2</sub> photodetector. *Adv Mater*, 2018, 30(43), 1803165
- Sang L W, Liao M Y, Sumiya M. A comprehensive review of semiconductor ultraviolet photodetectors: from thin film to one-dimensional nanostructures. *Sensors*, 2013, 13(8), 10482
- Li SY, Zhang Y, Yang W, et al. 2D perovskite Sr<sub>2</sub>Nb<sub>3</sub>O<sub>10</sub> for high-performance UV photodetectors. *Adv Mater*, 2020, 32(7), 1905443
- Konstantatos G, Levina, L, Fischer A, et al. Engineering the temporal response of photoconductive photodetectors via selective introduction of surface trap states. *Nano Lett*, 2008, 8(5), 1446
- Jin Y Z, Wang J P, Sun B Q, et al. Solution-processed ultraviolet photodetectors based on colloidal ZnO nanoparticles. *Nano Lett*, 2008, 8(6), 1649
- Zhao B, Wang F, Chen H Y, et al. An ultrahigh responsivity (9.7 mA W<sup>-1</sup>) self-powered solar-blind photodetector based on individual ZnO-Ga<sub>2</sub>O<sub>3</sub> heterostructures. *Adv Funct Mater*, 2017, 27(17), 1700264
- Kong W Y, Wu G A, Wang K Y, et al. Graphene- $\beta$ -Ga<sub>2</sub>O<sub>3</sub> heterojunction for highly sensitive deep UV photodetector application. *Adv Mater*, 2016, 28(48), 10725
- Chen X M, Liu K W, Zhang Z Z, et al. A self-powered solar-blind photodetector with fast response based on Au/ $\beta$ -Ga<sub>2</sub>O<sub>3</sub> nanowires array film Schottky junction. *ACS Appl Mater Inter*, 2016, 8(6), 4185
- Pratiyush A S, Krishnamoorthy S, Solanke S V, et al. High responsivity in molecular beam epitaxy grown  $\beta$ -Ga<sub>2</sub>O<sub>3</sub> metal semiconductor metal solar blind deep-UV photodetector. *Appl Phys Lett*, 2017, 110(22), 221107
- Posada F G, Songmuang R, Hertog M D, et al. Room-temperature photodetection dynamics of single GaN nanowires. *Nano Lett*, 2012, 12(1), 172
- Butuna B, Tut T, Ulker E, et al. High-performance visible-blind GaN-based p-i-n photodetectors. *Appl Phys Lett*, 2008, 92(3), 033507
- Xu G Y, Salvador A, Kim W, et al. High speed, low noise ultraviolet photodetectors based on GaN p-i-n and AlGaIn(p)-GaN(i)-GaN(n) structures. *Appl Phys Lett*, 1997, 71(15), 2154
- Zheng L X, Yu P P, Hu K, et al. Scalable-production, self-powered TiO<sub>2</sub> nanowell-organic hybrid UV photodetectors with tunable performances. *ACS Appl Mater Inter*, 2016, 8(49), 33924
- Li X D, Gao C T, Duan H G, et al. Nanocrystalline TiO<sub>2</sub> film based photoelectrochemical cell as self-powered UV-photodetector. *Nano Energy*, 2012, 1(4), 640
- Patel M, Kim H S, Kim J. All transparent metal oxide ultraviolet photodetector. *Adv Electron Mater*, 2015, 1(11), 1500232
- Chen Z, Li B R, Mo X M, et al. Self-powered narrowband p-NiO/n-ZnO nanowire ultraviolet photodetector with interface modification of Al<sub>2</sub>O<sub>3</sub>. *Appl Phys Lett*, 2017, 110(12), 123504
- Cai J, Xu X J, Su L X, et al. Self-powered n-SnO<sub>2</sub>/p-CuZnS core-shell microwire UV photodetector with optimized performance. *Adv Opt Mater*, 2018, 6(15), 1800213
- Xu X J, Shukla S, Liu Y, et al. Solution-processed transparent self-powered p-CuS-ZnS/n-ZnO UV Photodiode. *Phys Status Solidi RRL*, 2018, 12(2), 1700381
- Su L X, Zhang Q L, Wu T Z, et al. High-performance zero-bias ultraviolet photodetector based on p-GaN/n-ZnO heterojunction. *Appl Phys Lett*, 2014, 105(7), 072106
- Su L X, Zhu Y, Yong D Y, et al. Wide range bandgap modulation based on ZnO-based alloys and fabrication of solar blind UV detectors with high rejection ratio. *ACS Appl Mater Inter*, 2014, 6(16), 14152
- Moon T H, Jeong M C, Lee W, et al. The fabrication and characterization of ZnO UV detector. *Appl Surf Sci*, 2005, 240(1-4), 280
- Wang Z N, Yu R M, Wang X F, et al. Ultrafast response p-Si/n-ZnO heterojunction ultraviolet detector based on pyro-phototronic effect. *Adv Mater*, 2016, 28(32), 6880
- Liang S, Sheng H, Liu Y, et al. ZnO Schottky ultraviolet photodetectors. *J Cryst Growth*, 2001, 225(2-5), 110
- Pearton S J, Norton D P, Ip K, et al. Recent progress in processing and properties of ZnO. *Prog Mater Sci*, 2005, 50(3), 293
- Özgür A, Alivov Y I, Liu C, et al. A comprehensive review of ZnO and related devices. *J Appl Phys*, 2005, 98(4), 041301
- Shen H, Shan C, Li B, et al. Reliable self-powered highly spectrum-selective ZnO ultraviolet photodetectors. *Appl Phys Lett*, 2013, 103, 232112
- Cho H D, Zakirov A S, Yuldashev S U, et al. Photovoltaic device on a single ZnO nanowire p-n homojunction. *Nanotechnology*, 2012, 23(11), 115401
- Hu K, Teng F, Zheng L X, et al. Binary response Se/ZnO p-n heterojunction UV photodetector with high on/off ratio and fast speed. *Laser Photonics Rev*, 2017, 11(1), 1600257
- Chen H Y, Yu P P, Zhang Z M, et al. Ultrasensitive self-powered solar-blind deep-ultraviolet photodetector based on all-solid-state polyaniline/MgZnO bilayer. *Small*, 2016, 12(42), 5809
- Li J, Li H, Zhan G, et al. Solar water splitting and nitrogen fixation with layered bismuth oxyhalides. *Acc Chem Res*, 2017, 50(1), 112
- Huang X Y, Li B, Guo H. Synthesis, photoluminescence, cathodoluminescence and thermal properties of novel Tb<sup>3+</sup>-doped BiOCl green-emitting phosphors. *J Alloy Compd*, 2017, 695(25), 2773
- Zhang Y W, Xu X H, Xing Y, et al. Growth and electronic transport property of layered BiOCl microplates. *Adv Mater Interfaces*, 2015, 2(12), 1500194
- Dutta S, Das T, Datta S. Impact of bi-axial strain on structural, electronic and optical properties of photo-catalytic bulk bismuth oxy-

halides. *Phys Chem Chem Phys*, 2018, 20(1), 103

- [37] Dash A, Sarkar S, Adusumalli V N K B, et al. Microwave synthesis, photoluminescence, and photocatalytic activity of PVA-functionalized  $\text{Eu}^{3+}$ -doped  $\text{BiOX}$  ( $X = \text{Cl}, \text{Br}, \text{I}$ ) nanoflakes. *Langmuir*, 2014, 30(5), 1401
- [38] Li Y J, Wang Q, Liu B C, et al. The {001} facets-dependent superior photocatalytic activities of  $\text{BiOCl}$  nanosheets under visible light irradiation. *Appl Surf Sci*, 2015, 349(15), 957
- [39] Tripathi G K, Kurchania R. Photocatalytic behavior of  $\text{BiOX}$  ( $X = \text{Cl}/\text{Br}, \text{Cl}/\text{I}$  and  $\text{Br}/\text{I}$ ) composites/heterogeneous nanostructures with organic dye. *Opt Quant Electron*, 2017, 49(6), 203
- [40] Cheng H F, Huang B B, Dai Y. Engineering  $\text{BiOX}$  ( $X = \text{Cl}, \text{Br}, \text{I}$ ) nanostructures for highly efficient photocatalytic applications. *Nanoscale*, 2014, 6(4), 2009
- [41] Yu Y X, Ouyang W X, Zhang W D. Photoelectrochemical property of the  $\text{BiOBr-BiOI}/\text{ZnO}$  heterostructures with tunable bandgap. *J Solid State Electrochem*, 2014, 18(6), 1743
- [42] Teng F, Ouyang W X, Li Y M, et al. Novel structure for high performance UV photodetector based on  $\text{BiOCl}/\text{ZnO}$  hybrid film. *Small*, 2017, 13(22), 1700156



**Longxing Su** is a research assistant professor in School of Physical Science and Technology at ShanghaiTech University, China. He received his joint-supervised Ph.D. degree from the Sun Yat-Sen University and UC Riverside in 2015. His current research topic mainly focuses on inorganic/organic semiconductor based optoelectronic devices, photoelectronic synergetic catalysis, and power devices.



**Xiaosheng Fang** is currently a professor in the Department of Materials Science, Fudan University, China. His current research involves the controlled fabrication, novel properties, and optoelectronic applications of inorganic semiconductors, especially with a focus on II-VI inorganic semiconductors and high-performance UV photodetectors.